Magnetic coupling between high magnetization perpendicular electrodes in an epitaxial FePt/MgO/FePt magnetic tunnel junction

P. de Person, P. Warin,* M. Jamet, C. Beigne, and Y. Samson
CEA-Grenoble/Département de recherche fondamentale sur la matière condensée/Service de Physique des Matériaux et des Microstructures, 17 rue des martyrs, 38054 Grenoble Cedex 09, France
(Received 20 April 2007; published 1 November 2007)

In this paper, we investigate the magnetic coupling between perpendicularly magnetized FePt electrodes in a fully epitaxial FePt/MgO/FePt magnetic tunnel junction grown by molecular beam epitaxy. The epitaxial growth is monitored *in situ* by reflection high energy electron diffraction and *ex situ* using x-ray diffraction and transmission electron microscopy. Despite the large magnetization of FePt (leading to high stray fields) and the thinness of the tunnel barrier, we do not observe magnetic coupling between the electrodes in major hysteresis loops or when reversing the soft electrode alone. However, the magnetization reversal of the soft layer (SL) strongly depends on the remanent state of the hard layer (HL), ending with full magnetic coupling between the electrodes and a single magnetization reversal for the zero-remanence state. We have closely related macroscopic magnetic measurements performed using the magneto-optical Kerr effect with microscopic observations of magnetic domains performed by magnetic force microscopy. In the coupling regime, the domain wall propagation in the soft layer is driven by the magnetic domain configuration of the hard layer. Indeed, the HL domain wall stray field becomes larger than the pinning field over structural defects in the SL.

DOI: 10.1103/PhysRevB.76.184402 PACS number(s): 75.70.Kw, 75.60.Jk, 75.47.−m, 75.50.Bb

I. INTRODUCTION

Magnetic trilayers now correspond to a rich and growing area of physics. These are thin film structures where the magnetization of two magnetic layers—separated by a non magnetic spacer—can be independently controlled. These magnetic trilayers find widespread applications since the introduction of the spin valves, where the spacer is a nonmagnetic metal. The spin valves provided the way to use giant magnetoresistance phenomena practically in hard disk recording heads. Recently, the focus shifted to magnetic tunnel junctions (MTJs) that are at the core of magnetic random access memories.[1,2] MTJs can be used as highly sensitive sensors for field detection applications, included in hard disk recording heads.

As a matter of fact, magnetic trilayers were originally developed with in-plane magnetization. As one key requirement for any application is the ability to control independently the magnetization of the two ferromagnetic layers, numerous studies focused on the magnetic coupling phenomena between the two ferromagnetic layers. It has been observed that repeated field cycling of the magnetization of the soft electrode finally affects (demagnetizes) the hard layer in in-plane tunnel junctions.[3] This progressive demagnetization was explained by the large magnetic stray field created at the apex of the domain walls created within the soft layer during magnetization reversal.[3,4] In magnetoresistive devices, such an effect would have damaging consequences such as the loss of information or efficiency.

Systems with perpendicular magnetization have been far less studied. Nevertheless, the continuous shrinking of the size of all kind of spintronic devices makes perpendicular systems increasingly attractive. Indeed, the perpendicular magnetization ends up with specific advantages,[5] and the perpendicular geometry also eases the introduction of high anisotropy materials that are required to push down the superparamagnetic limit.[6] Only recently, reports have been published on domain-wall-induced coupling phenomena within systems with perpendicular magnetization, such as Pt/Co-based spin valves.[7]

Achieving full decoupling between two perpendicular electrodes separated by a thin spacer is by no means an easy task. In thin films with perpendicular magnetization, magnetization reversal occurs through domain nucleation and domain wall propagation. As a result, the most desirable reversal process, coherent rotation of the magnetization, is not practically observed in the case of electrodes with large perpendicular anisotropy. Large stray fields are created in the vicinity of domain walls or above small enough magnetic domains. Wiebel *et al.* showed that stray fields lead to a wealth of new and interesting physical phenomena: e.g., the dipolar coupling between the two electrodes can provoke domain decoration.[7,8]

Here, we extend magnetic coupling observations to high perpendicular anisotropy electrodes with high magnetization at saturation (compared with Co/Pt multilayers) namely, FePt thin films ($M_s \sim 1100$ kA m^{-1}, $K_u \sim 5\times 10^6$ J m^{-3}).[9] The two magnetic layers are separated by a thin (3 nm) epitaxial MgO(001) tunnel barrier. Such MgO barriers have been shown to exhibit spectacularly large amplitude of tunnel magnetoresistance with specific electrodes such as Fe or FeCo due to spin filtering effects.[10–13] Here, we show that it is possible to prepare a fully epitaxial FePt/MgO/FePt trilayer. The large magnetic anisotropy originates from high uniaxial chemical ordering of both FePt electrodes in the $L1_0$ phase. We combined magneto-optical Kerr effect measurements and magnetic force microscopy (MFM) to understand and image the magnetic configurations of both FePt electrodes upon magnetization reversal. We then get a detailed description of the processes leading to coupling or decoupling upon magnetization reversal as a function of the magnetization state of each electrode.

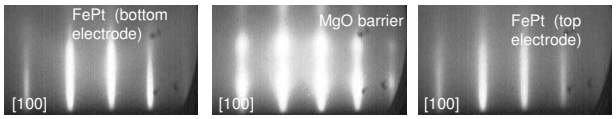

FIG. 1. RHEED patterns recorded at the end of the growth of each layer: (left) 5-nm-thick bottom FePt electrode, (middle) 3-nm-thick MgO(001) barrier, (right) 10-nm-thick FePt top electrode. The images have been obtained along the [100] azimuth, the absence of superstructure peaks indicates the absence of FePt parts with in-plane *c* axis

II. GROWTH AND STRUCTURAL CHARACTERIZATION

FePt(10 nm)/MgO(3 nm)/FePt(x nm)/Pt(001)/MgO(001) (substrates) stackings were grown. If not explicitly stated, the results presented in this paper concern MTJ samples with $x=5$ nm. To investigate the role of the thicknesses of the magnetic layers, specific samples, with different values of x, have been prepared by progressively masking the sample by a mechanical shutter. This process minimizes any dispersion of the sample properties due to the growth conditions. The Pt(001) buffer was obtained on a thin Cr (3 nm) seed layer as described in a previous paper.[14] The bottom FePt electrode was grown by coevaporating both Fe and Pt elements from two independent *e* guns on the Pt(001) buffer held at 770 K. The alloy growth rate was 0.06 nm s^{-1}. The MgO(001) barrier was grown by *e*-beam evaporation from a high quality MgO material source (crushed MgO substrates), using a two-step process ending at 770 K. The top FePt electrode was grown using a two-step process: first a $[\text{Fe(1 ML)/Pt(1 ML)}]_6$ multilayer was formed ML indicates multilayer at 443 K, followed by an annealing at 770 K, ending with a coevaporation of both elements on the sample held at 770 K. Finally, a 3-nm-thick Pt capping was added to protect the sample from oxidation. Reflection high energy electron diffraction (RHEED) demonstrated a high quality epitaxial growth of the FePt(001) upper and bottom electrodes, and of the MgO(001) barrier (Fig. 1).

X-ray diffraction (XRD) confirmed the coherent growth of each ferromagnetic electrode, and the high uniaxial chemical ordering ordered in the $L1_0$ phase [Fig. 2(a)]. The FePt(00k) peaks associated with each electrode can be separated, revealing different lattice parameters for both electrodes. Indeed, the bottom FePt layer grows pseudomorphically strained on the Pt buffer layer (in-plane lattice parameter $a_{\text{FePt,SL}}=0.392$ nm), whereas the top FePt layer grows fully relaxed on the MgO tunnel barrier [$a_{\text{FePt,HL}}=0.386$ nm, a value very close to the bulk one (0.385 nm)[15]]. It is then possible to determine the chemical order parameter (S) of each FePt electrode. S was estimated from the ratio of the (001) and (003) peaks (both linked to the $L1_0$ superstructure) to the fundamental (002) and (004) ones:[16] $S_{\text{FePt,SL}}=0.8\pm0.1$ for the thin bottom electrode and $S_{\text{FePt,HL}}=0.6\pm0.1$ for the thicker top electrode. The main source of uncertainty on S originates from the overlap between the peaks associated with the two electrodes.

Further knowledge of the sample structure was gained by transmission electron microscopy [Fig. 2(b)]. Images demonstrate both the flatness and the good crystallinity of the

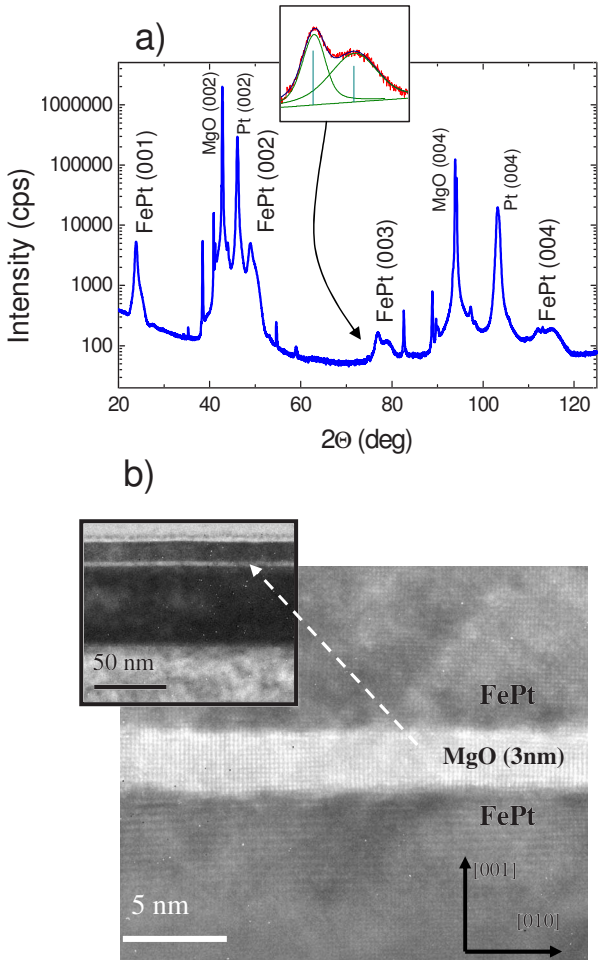

FIG. 2. (Color online) (a) θ-2θ scan of the FePt(10 nm)/MgO(3 nm)/FePt(5 nm)/Pt(001)/MgO(001) stacking (obtained using Cu $K\alpha$ radiation; the peaks at 38°, 40°, 82°, and 88° correspond to Cu $K\beta$ ones associated with Pt or MgO). (b) Transmission electron microscopy micrograph of a similar FePt/MgO(3 nm)/FePt stacking (cross section).

MgO(001) barrier. Pinholes within the MgO barrier have never been observed on the images. The large lattice mismatch between the in-plane MgO lattice parameter and the FePt one (9%) is fully relaxed by interface dislocations (typically, one dislocation is observed every 13 atomic planes). Misfit dislocations are also clearly seen in the top FePt electrode at the upper FePt/MgO interface. These latter dislocations lead to the full relaxation of the top FePt electrode indicated by XRD measurements.

All hysteresis loops were measured at room temperature using the polar magneto-optical Kerr effect (PMOKE). Vibrating sample magnetometry (VSM) was specifically used to get quantitative magnetization values. The major loop associated with the FePt(10 nm)/MgO(3 nm)/FePt(5 nm)/Pt(100) MTJ structure exhibits two well-separated magnetization reversals. It is then possible to create both the parallel and antiparallel magnetic configurations [Fig. 3(a)]. Both magnetic configurations are stable once back in zero field.

Providing absolute magnetization values, the VSM data indicate that the bottom electrode [FePt(5 nm)/Pt] and the

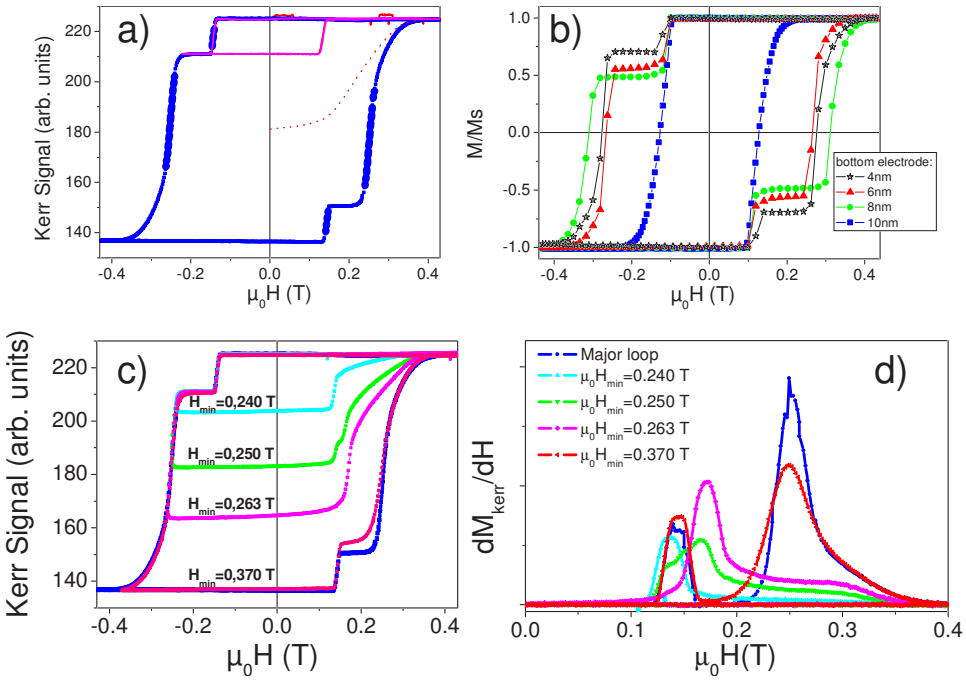

FIG. 3. (Color online) Hysteresis loops of the magnetic tunnel junctions, measured by polar magneto-optical Kerr effect (applied field along the perpendicular axis). (a) FePt(10 nm)/MgO(3 nm)/FePt(5 nm)/Pt(001). The dashed line corresponds to the virgin state magnetization curve of the as-grown sample, the minor loop to the reversal of the soft electrode alone. (b) FePt(10 nm)/MgO(3 nm)/FePt(x nm)/Pt(001), for x=4, 6, 8, and 10 nm. A single reversal event (magnetic coupling) is observed when the thickness of the soft electrode is equal to or greater than 10 nm. (c) Major and minor hysteresis loops of the FePt(10 nm)/MgO(3 nm)/FePt(5 nm)/Pt(001) tunnel junction. Each loop starts at $\mu_0 H$=0.43 T, the field is next decreased down to $\mu_0 H_{\min}$, and next brought back to 0.43 T. (d) Derivative of the major and minor hysteresis loops in Fig. 3(c).

top electrode [FePt(10 nm)/MgO] correspond, respectively, to the soft (SL) and hard (HL) layers. The magnetization observed at the saturation field amounts to M_s=1100 kA/m, a figure similar to the expected value [1140 kA/m for $Fe_{0.5}Pt_{0.5}$ (Ref. 6)]. As the top electrode has the lower chemical order, and so the lower magnetocrystalline anisotropy, it can be deduced that its higher coercivity is linked to the presence of various structural defects pinning domain wall propagation. Results, such as MFM images, described in further parts of the paper support this conclusion.

Interestingly, minor loops can be used to cycle the soft electrode alone [Fig. 3(a)]. This decoupling between the two FePt electrodes is quite remarkable because a rough analysis would lead to the conclusion that the two electrodes should be coupled. Indeed, both electrodes have a large magnetization, and propagating domain walls then create a large stray field across the thin MgO barrier during magnetization reversal. It seems, however, that it is more complex than this simple analysis of the VSM data. Noticeably, the virgin state magnetization curve [Fig. 3(a), dashed line] exhibits a single reversal step, suggesting magnetic coupling between the two electrodes. Furthermore, the MFM images of a demagnetized sample show a single-domain configuration (full domain mirroring) with an average domain size of 330 nm (images not displayed here). Later in this paper, we show that MFM provides unambiguous images of domains in both layers when the magnetic configurations of the two electrodes differ. Magnetic coupling or decoupling can then be observed depending on the magnetic history of the sample.

III. ONE-ELECTRODE REVERSAL

To support the discussion, we have investigated the magnetization reversal of the soft electrode alone. We prepared a specific sample, corresponding to the bottom part of the full tunnel junction: MgO(3 nm)/FePt(5 nm)/Pt(001). Kerr and MFM data give evidence of a sharp magnetization reversal, proceeding mainly by domain wall propagation from very sparse nucleation events: a single reversed domain is observed on most MFM images (typically 40 μm wide), and reversed domains are experimentally never observed below the reversal field. Such images are very similar to the ones of Figs. 4(a) and 4(b). It is worth noting that the coercive field ($\mu_0 H_c$) is similar to the one obtained when this layer is a part of the full magnetic tunnel junction. Even if a very small effect would be difficult to demonstrate—as $\mu_0 H_c$ varies slightly from sample to sample—this means that the (saturated) hard layer has no significant effect upon the magnetization reversal of the soft layer. Here, it can be recalled that a perfectly flat, infinite, and perpendicularly magnetically saturated thin layer does not create any stray field. This can be understood by analogy to a capacitor.

Finally, we get an estimation of the equilibrium size of the magnetic domain by demagnetizing the single soft electrode within an oscillating field of decreasing amplitude: large magnetic domains, with a typical size around 3 μm, are observed by MFM. Such a large size was expected as the equilibrium size of magnetic domains in thin films with a large perpendicular anisotropy [$2K_u/(\mu_0 M_s^2) > 1$] increases expo-

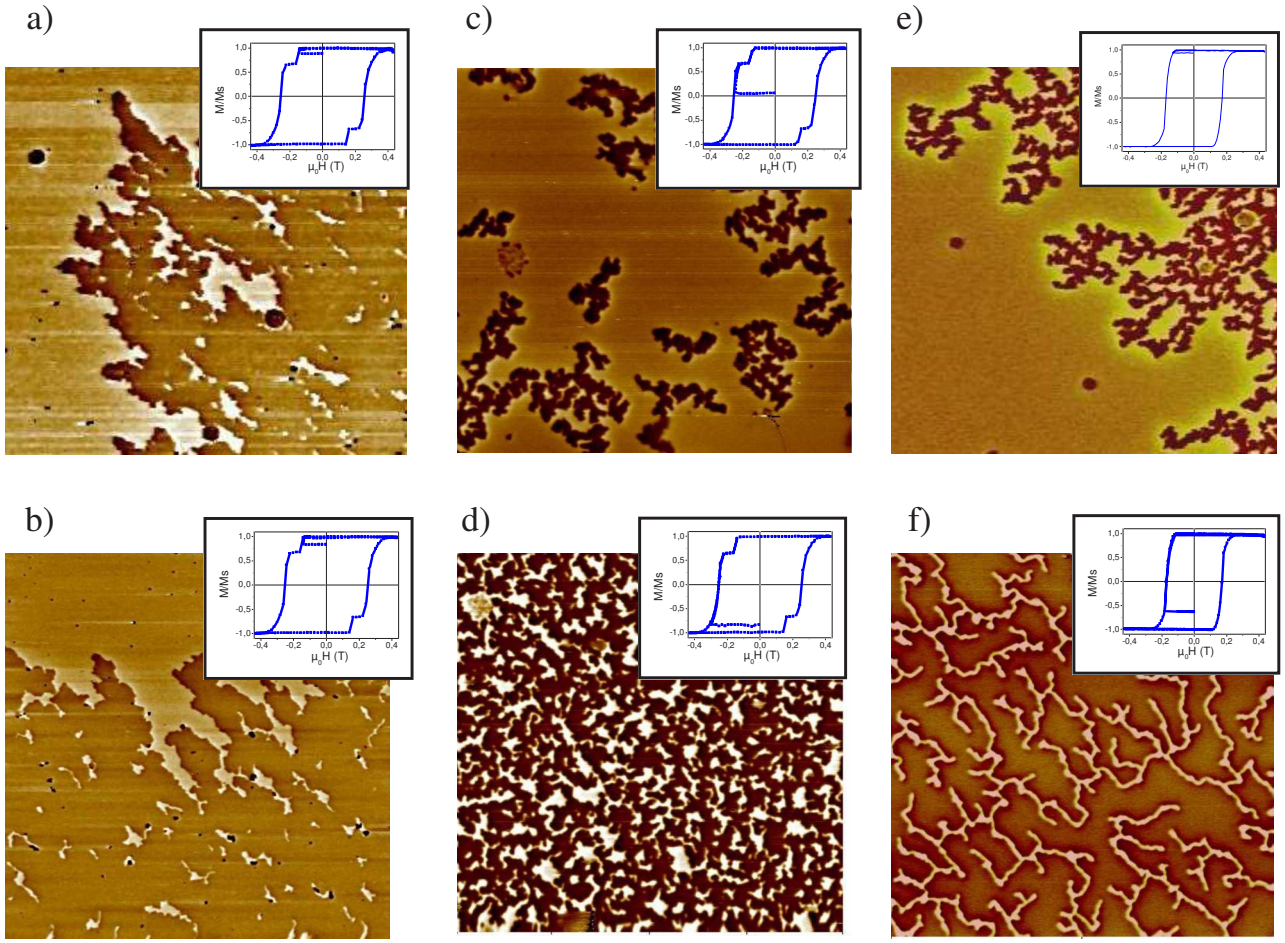

FIG. 4. (Color online) Magnetic force microscopy images recorded at zero field, the magnetic pattern being created as indicated in the inset. On all images, down magnetization corresponds to a darker pattern, all loops starting from a saturating positive field (up). The [100] direction is along the horizontal axis. (a)–(d) Images obtained on the FePt(10 nm)/MgO(3 nm)/FePt(5 nm) stacking. (a),(b) 20 μm images of the magnetization reversal of the soft layer, the applied field being too low to affect the hard layer. The reversed domain propagates in the soft layer from the left part of the images. In the upper right corners, both layer magnetizations are still up. (c),(d) 10 μm images of the magnetization reversal of the hard layer. The soft layer has its magnetization saturated along the down direction. (e),(f) 20 μm images and hysteresis loops obtained with a thicker bottom electrode: FePt(10 nm)/MgO(3 nm)/FePt(10 nm).

nentially when the layer thickness decreases,[14,17] leading to very large domain sizes at the thickness considered here (5 nm). Also, the equilibrium size of magnetic domains should be far lower in the comparatively thick (10 nm) hard electrode—this will be confirmed later by MFM images of the hard layer at various stages of magnetization reversal. As we will see later, the stray fields localized at the apex of the domain walls are instrumental in creating coupling or decoupling conditions between the two ferromagnetic electrodes. The large difference between the domain wall densities observed in the two electrodes will then deeply affect the magnetization reversal processes (in coupling conditions).

We can now focus on the magnetic configurations of both electrodes at intermediate stages of the magnetic reversal process. Our goal is to understand the underlying phenomena controlling coupling or decoupling between the two ferromagnetic layers. We relied on the fact that the magnetizations of both layers remain unchanged when going back to zero field from any stage of magnetization reversal [Fig. 3(c)]. We applied the following experimental procedure. The sample was first saturated in a large positive magnetic field, $\mu_0 H_{\mathrm{sat}} = +0.43$ T, next the field was decreased down to a given negative value $\mu_0 H_{\mathrm{min}}$, and finally set to zero. The reversal process is then frozen at a given stage and the sample can be observed by magnetic force microscopy. In the MFM images presented later, we are able to distinguish whether domains belong to the soft layer or to the hard layer by considering their shape, their size, and the magnetic history of the sample.

Let us start with $\mu_0 H_{\mathrm{min}}$ values corresponding to a partial reversal of the soft electrode: all images show the propagation of a single domain, with a dendritic shape, the domain wall being locally aligned along the [110] directions [Figs. 4(a) and 4(b)]. Such a shape originates from a large disorder in the sample.[18] Indeed, strongly pinning defects control the propagation path of the domain wall. Generally speaking, the shape of a domain wall is driven by a competition between the domain wall elasticity (associated with the cost of additional domain wall length), which tends to straighten the domain wall, and, locally, domain wall pinning on defects (lo-

cally pinning the domain wall by lowering its energy). The sample disorder corresponds to the distribution of these defects. Here, the anisotropic shape of the domain wall can be ascribed to pinning on microtwins.[9] The microtwins are strain relaxation defects extending along the [110] directions; they result from the pileup of partial dislocations gliding on {111} planes.[19] Some small unreversed areas are left behind the propagating domain wall [Figs. 4(a) and 4(b)], another clue to the large amplitude of the disorder. A few magnetization defects of the hard layer—appearing as dark bubbles—also locally affect the domain wall propagation in the soft layer. This is the only indication of any influence from the hard layer. It can then be concluded that the soft layer reversal is controlled by its own intrinsic parameters.

Both the hysteresis loops and the MFM images [Figs. 3(a) and 4] show that the magnetization reversal of the hard layer takes place only after the complete reversal of the soft layer. Imaging the domain pattern at intermediate stages of magnetization reversal of the hard layer [Figs. 4(c) and 4(d)—the soft layer being saturated along the down direction] reveals once again a process dominated by domain wall propagation. There is nevertheless a far larger number of nucleation sites: typically 1 per 10 μm^2 in the hard layer [from Fig. 4(c)], vs fewer than 1 per 10000 μm^2 in the soft layer (as confirmed by 100 μm MFM images, not shown here). This could correspond to weaker magnetocrystalline anisotropy in the hard layer. Indeed, the x-ray diffraction data indicated a weaker chemical order for the hard layer ($S_{HL}=0.6, S_{SL}=0.8$). Hence, the larger number of nucleation events within the hard layer can be linked to a lower domain wall energy (resulting in a lower energy barrier preventing bubble formation[20]), and maybe also to different crystalline defects locally easing bubble nucleation. The magnetic pattern exhibits a dendritic appearance, without strong directional anisotropy, and the average domain size is significantly lower than in the soft layer, around 300 nm (as expected due to the higher layer thickness).

To gain further experimental insight into the underlying mechanism creating the magnetic coupling, we grew samples with different thicknesses of the soft layer. When increasing the thickness of the soft layer, we observed a transition from well separated to coupled reversal processes in the major hysteresis loops of the trilayer. When the thickness of the soft layer is low enough, the two electrodes exhibit well-differentiated reversals. Conversely, for soft layer thicknesses $x=10-12$ nm (depending on the sample) and above, the two electrodes reverse simultaneously [see Fig. 4(b)]. Interestingly, both the nucleation and the coercive fields correspond to the ones observed for the reversal of the SL in major hysteresis loops. This indicates that the reversal process is controlled by the SL, where the first domains propagate and induce the simultaneous reversal of the HL. As expected, reducing or increasing the thickness of the top (hard) electrode has no similar effect.

The top electrode has the lower chemical order, and so the lower magnetocrystalline anisotropy. Nevertheless, the coercivity (here mainly related to domain wall propagation and not the nucleation), is mainly linked to the strength of structural defects pinning domain walls. Here, we indeed expect different microstructures for the two FePt layers, one being grown on a relatively flat Pt(001) buffer, with a small misfit, the second one on a thin MgO layer (fully relaxed as shown by RHEED patterns taken during MgO growth) with a larger misfit. The strong influence of these different miscrostructures on domain wall propagation phenomena appears strikingly on the MFM images displayed later in this paper. To conclude, these structural differences are more important here than the limited reduction in the magnetocrystalline anisotropy associated with a lower chemical order parameter in the top FePt layer, and they explain why the top electrode exhibits the higher coercivity.

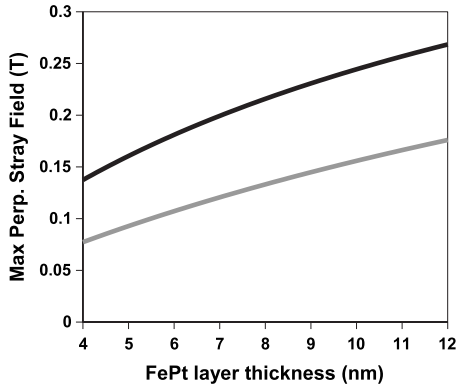

FIG. 5. Maximum value of the perpendicular stray field (in T) created in the vicinity of a domain wall from a FePt layer with a given thickness (4–12 nm). Black curve: at 3 nm from the FePt layer surface. Gray curve: at 8 nm from the FePt layer surface. The magnetization profile in the domain wall was approximated by an arctangent function.

Using a continuous model and arctangentlike domain wall profile, it is possible to calculate the stray field created by one layer on the other. This stray field is the largest in the vicinity of the magnetic domain walls. Given the perpendicular magnetization of both electrodes, it is likely that the perpendicular component of the stray field is the most instrumental in inducing domain nucleation or domain wall propagation. We then calculated the stray field created at mid-thickness of the second electrode by an equilibrium domain wall structure in the first electrode. The domain wall width is close to 4 nm. Figure 5 shows that the stray field created by a domain wall increases rapidly with the layer thickness, with values in the 0.15–0.2 T range within the second electrode.

Combined with the external field required to reverse the soft layer, such stray field values are high enough to reach the coercive field of the hard layer. It is then likely that the domain walls are at the origin of the magnetic coupling observed when increasing the thickness of the soft layer. Added to the fact that the stray field increases with the layer thickness (Fig. 5), there is the additional effect that the magnetic domain get smaller with higher layer thicknesses. Indeed, even if thin layers are not at equilibrium during magnetization reversal, the average domain size at the coercive field is close to the equilibrium one. As a result, thicker films lead to smaller domains and a more intense field is created over larger parts of the second electrode. Imaging by MFM a FePt(10 nm)/MgO(3 nm)/FePt(10 nm) trilayer after minor

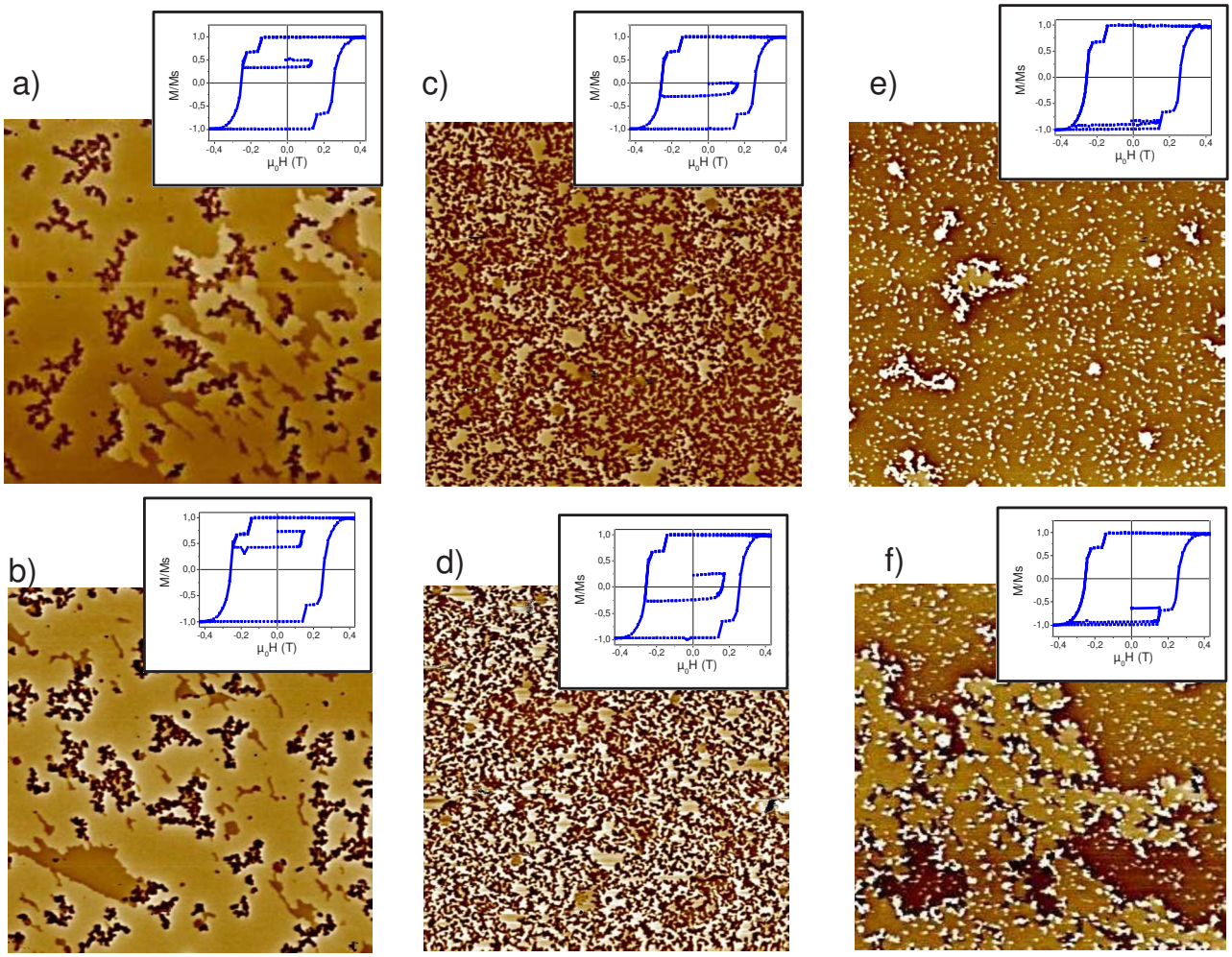

FIG. 6. (Color online) Magnetic force microscopy images recorded at zero field, the magnetic pattern being created as displayed in the inset. The sample is first saturated at 0.43 T prior to applying a negative field, and comes back to zero field after inducing a partial reversal of the soft layer. The [100] direction is along the horizontal axis. From left to right, images correspond to a very partially reversed hard layer (a),(b), an approximately demagnetized hard layer (c),(d), and an almost reversed hard layer (e),(f). In the upper images (a),(c),(e), the soft layer reversal is very partial. In the bottom images (b),(d),(f), the soft layer reversal has been pushed closer to completion. The up domain propagating within the soft layer appears as a large bright area. Reversed domains in the hard layer (down) appear as black ones. In images (e),(f) the reversed domain has invaded the hard layer almost completely; the most intense contrast (white) now corresponds to remaining down areas within the hard layer.

loops [Figs. 4(e) and 4(f)] reveals a single magnetic contrast. This is indicative of full domain mirroring (magnetic coupling) even at the microscopic scale.

IV. MAGNETIC COUPLING INDUCED BY A PARTIALLY REVERSED ELECTRODE

We now turn toward the influence of intermediate states of magnetization of the hard layer (the thickest one, which then creates the higher stray field) on the magnetization reversal of the soft layer. The sample [FePt(10 nm)/MgO(3 nm)/FePt(5 nm)] was first saturated by applying $\mu_0 H_{sat} = +0.43$ T; next the applied field was decreased down to a given negative value $\mu_0 H_{min}$ corresponding to a partial magnetization reversal of the hard layer. The field was next increased either up to saturation to get the hysteresis loops displayed in Fig. 3(c) or up to a field $\mu_0 H_{final}$ corresponding to an intermediate stage of magnetization reversal of the soft layer. Imaging by MFM these latter magnetic configurations provided a unique insight into the reversal process (Fig. 6).

A. Beginning of hard layer reversal

Experimental data then reveal the existence of three main coupling behaviors, depending on the magnetization of the hard layer (controlled by $\mu_0 H_{min}$). The first one corresponds to a reversal process stopped at an early stage in the hard layer [see $\mu_0 H_{min} = 0.240$ T in Fig. 3(c)]. As shown more clearly in the derivatives of the hysteresis curves [Fig. 3(d)], the magnetization reversal of the trilayer proceeds in two steps. The first step corresponds to a sharp reversal, the associated coercive field $\mu_0 H_c = 0.133$ T being equal to the one observed in minor loops of the soft layer [Fig. 3(a)]. It then

seems that the magnetization reversal of the hard layer occurs progressively—in a second step—at higher fields. MFM images [Figs. 6(a)–6(c)] provide a clear explanation of these macroscopic data. The magnetization reversal in the soft layer proceeds mainly by domain wall propagation from a few nucleation centers [only one in Fig. 6(a)]. Nevertheless, the images give evidence of local pinning of the large domain wall propagating in the soft layer at the border of the domains nucleated in the hard layer. To our knowledge, such a phenomenon has not been observed up to now, and can be described as the propagation of the soft layer domain wall within the additional disorder created by the stray fields from the hard layer. These stray fields act as an additional source of disorder, added to the structural disorder already described. Basically, the intense up-field created at the external border of the hard layer down domains [black ones in Figs. 6(a) and 6(b)] stabilizes the propagating domains in the soft layer. In addition, the large down field created at the internal border of the same down domains opposes further propagation of the up domain within the soft layer. This process locally leads to domain decoration (as the border of the up domain propagating in the soft layer follows locally the limits of the domains in the hard layer). Nevertheless, even if the local influence of the HL is obvious on MFM images, it is not large enough to significantly change macroscopic parameters such as the coercive field corresponding to the soft layer reversal. This can be easily explained: at this very partial stage of the magnetization reversal of the hard layer, the reversed domains occupy a small fraction of the surface. As a result, the pinning of the domain wall (soft layer) by the hard layer occurs only locally, leaving ample space for the domain wall to propagate freely in the soft layer. Figure 6(b) indeed shows that increasing slightly the up field applied ($\mu_0 H_{\text{final}}$) ends with further invading of the soft layer by the reversed domain. It is no longer possible to determine the magnetic configuration below the down domains nucleated in the hard layer. However, these latter domains are at least fully surrounded by the large up domain propagating in the soft layer, implying that they do not heavily affect magnetization reversal.

B. Hard layer half reversed

The second case is observed when the hard layer has been approximately demagnetized (50% reversal) by the application of $\mu_0 H_{\text{min}}$ [−0.263 T in Figs. 6(c) and 6(d)]. The reversal process then observed when increasing the magnetic field consists of a single event: the value of the corresponding coercive field—between 0.16 and 0.17 T—is progressively enhanced with respect to the case of a partially reversed hard layer [Figs. 6(a) and 6(b)]. Interestingly, this coercive field increases with larger $|\mu_0 H_{\text{min}}|$ (with further magnetization reversal of the hard layer). This is observed up to values of $\mu_0 H_{\text{min}}$ corresponding to a 75% reversal of the hard layer (Fig. 7). Next, the coercive field progressively returns to the values observed for the reversal of the soft layer in major loops. As the hard layer has a magnetization value close to zero [Figs. 6(c) and 6(d)], the MFM images give evidence of a large density of domain walls within the hard layer. These

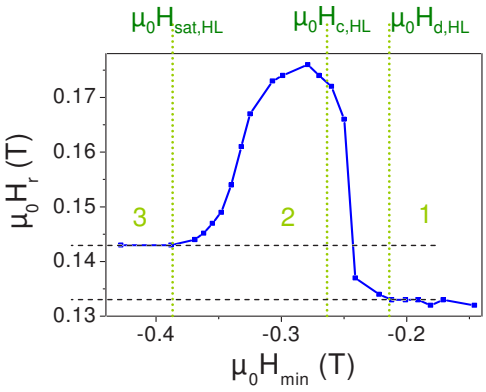

FIG. 7. (Color online) Evolution of the field $\mu_0 H_r$ corresponding to the first reversal event when increasing the applied field from a negative value $\mu_0 H_{\text{min}}$. All measurements started with the application of a 0.43 T saturating and positive field. The displayed values are obtained from the maximum of the derivative [as in Fig. 3(d)] of the magnetization curve [Fig. 3(c)].

domain walls (hard layer) strongly affect the propagation path of the domain wall within the soft layer. In other words, the additional disorder introduced by the stray fields from the magnetic pattern in the hard layer now strongly dominates over the structural disorder within the soft layer [Figs. 6(c) and 6(d)]. As a result, the domain wall morphology (soft layer) has radically changed with respect to the case of the saturated hard layer electrode [Figs. 4(a) and 4(b)] or even the case of a very partial reversal of the HL [Figs. 6(a) and 6(b)]. Now, the domain wall within the soft layer propagates across an intense and spatially disordered stray field pattern. This results in a unique and original domain wall shape as the propagating domain wall finds a path across the stray field from the fractal magnetic pattern of the hard layer [Fig. 6(c)].

A quantitative analysis can be proposed. The typical values of pinning fields over structural defects within the soft layer can be overestimated by the coercive field of the layer (0.133 T).[18] Such pinning field values are lower than the stray fields created within the soft layer by magnetic domain walls from the hard layer (typically 0.2 T; Fig. 5). The domination of the magnetic disorder over the structural one can then be understood. This large influence of the stray field disorder also allows us to understand how starting from a partial reversal of the hard layer can significantly enhance the field $\mu_0 H_r$, defined as the maximum of the differentiation of the magnetization curve associated with the first reversal event observed when increasing the applied field (Fig. 7). Indeed, local domain wall pinning over reversed domains within the hard layer pushes the percolation field of the soft layer toward higher values. Obviously, this is true only when a significant part of the surface is occupied by reversed domains in the hard layer. When only a small fraction of the hard layer is occupied by reversed domains, the domain wall propagating in the soft layer finds an easy path within the large unreversed areas. We then understand qualitatively the shape of the curve displayed in Fig. 7.

Intermediate cases are then expected and observed at intermediate stages of the magnetization reversal of the hard

layer. Such a case corresponds to $\mu_0 H_{min} = -0.250$ T [see the hysteresis loop in Fig. 3(c)]. The derivative of the magnetization curve can then be fitted with three contributions, respectively on 0.134 T (coercive field of the soft layer, $\mu_0 H_{c,SL}$), 0.162 T, and 0.239 T (coercive field of the hard layer, $\mu_0 H_{c,HL}$). It is then likely that the reversal process of the soft layer starts with nucleation and easy domain wall propagation across unreversed parts of the hard layer. In order to fully reverse the soft layer, the propagating domain has to invade it completely. The propagating domain wall is probably first locally pinned by the stray field from the hard layer. If the domain wall density is too large in the hard layer, the domain wall cannot find an easy propagation path. Therefore magnetization reversal is blocked. Next, at higher applied field the domain wall propagates again and its own stray field pushes the domain wall in the hard layer (inducing locally magnetization reversal in the hard layer). This mechanism gives rise to a coupled reversal process.

C. Hard layer nearly reversed

The third and last case corresponds to the reversal of the soft layer when starting with an almost reversed hard layer [see $\mu_0 H_{min} = -0.370$ T in Figs. 3(c) and 3(d)]. It may appear rather similar—by symmetry—to the first one, where the starting configuration was a hard layer just beginning its reversal. Indeed, the domain wall (in the soft layer) also propagates across the stray field disorder from the small domains remaining in the hard layers. Nevertheless, the shape of these small domains [Fig. 6(e) and 6(f)], which corresponds to the remaining part of the up magnetization that almost collapsed, differs from the morphology of the down domains nucleated at the beginning of the hard layer magnetization reversal [Figs. 6(a) and 6(b)]. This difference ends up with a higher wall roughness in the soft layer. Also, it can be noticed that the size of the remaining up domains in the hard layer has been increased at the border of the domain wall from the soft layer (compared to the size of unaffected white domains out of the area covered by the domain wall). This evolution can be ascribed to magnetostatic effects.

V. CONCLUSION

Summarizing this study, we demonstrated the feasibility of high magnetic anisotropy perpendicular magnetic tunnel junctions. In spite of the large intrinsic magnetization of the FePt electrodes and of the small thickness of the spacer (3 nm MgO), magnetic decoupling can be achieved as observed in major hysteresis loops. Generally speaking, full decoupling is observed when attempting to reverse the magnetization of one electrode, the second one being saturated. In this case, the magnetization of either electrode can be stabilized at any given value.

Next, we have shown that magnetic coupling or decoupling can be observed depending on the magnetization states of both electrodes. The stray field localized at the vicinity of magnetic domain walls is instrumental in the creation of the magnetic coupling between the electrodes. This is demonstrated by both magnetic force microscopy images and a quantitative comparison of the domain wall stray field amplitude vs the pinning field over structural defects controlling domain wall propagation in each layer. When imaging the magnetic patterns associated with the magnetic coupling, we uncovered a wealth of new and original domain wall geometries. These geometries originate in each electrode from the combination of the structural disorder and of the additional disorder introduced by the stray field from the second electrode.

ACKNOWLEDGMENTS

We express our most profound thanks to J.-C. Pillet, L. Notin, and P. Montmayeul for technical support on the growth of the samples and PMOKE setup. We also thank E. Bellet-Amalric for specific XRD measurements.

*Corresponding author. patrick.warin@cea.fr

[1] S. A. Wolf, D. D. Awschalom, R. A. Buhrman, J. M. Daughton, S. von Molnár, M. L. Roukes, A. Y. Chtchelkanova, and D. M. Treger, Science **294**, 1488 (2001).
[2] J. Kerman, Science **308**, 508 (2005).
[3] L. Thomas, M. G. Samant, and S. S. P. Parkin, Phys. Rev. Lett. **84**, 1816 (2000).
[4] W. Kuch, L. I. Chelaru, K. Fukumoto, F. Porrati, F. Offi, M. Kotsugi, and J. Kirschner, Phys. Rev. B **67**, 214403 (2003).
[5] N. Nishimura, T. Hirai, A. Koganei, T. Ikeda, K. Okano, Y. Sekiguchi, and Y. Osada, J. Appl. Phys. **91**, 5246 (2002).
[6] D. Weller and A. Moser, IEEE Trans. Magn. **35**, 4423 (1999).
[7] S. Wiebel, J. Jamet, N. Vernier, A. Mougin, J. Ferré, V. Baltz, B. Rodmacq, and B. Dieny, Appl. Phys. Lett. **86**, 142502 (2005).
[8] B. Rodmacq, V. Baltz, and B. Dieny, Phys. Rev. B **73**, 092405 (2006).
[9] J. P. Attane, Y. Samson, A. Marty, D. Halley, and C. Beigne, Appl. Phys. Lett. **79**, 794 (2001).
[10] M. Bowen *et al.*, Appl. Phys. Lett. **79**, 1655 (2001).
[11] E. Popova *et al.*, Appl. Phys. Lett. **81**, 1035 (2002).
[12] S. S. P. Parkin, C. Kaiser, A. Panchula, P. Rice, B. Hughes, M. Samant, and S. Yang, Nat. Mater. **3**, 862 (2004).
[13] S. Yuasa, T. Nagahama, A. Fukushima, Y. Suzuki, and K. Ando, Nat. Mater. **3**, 868 (2004).
[14] V. Gehanno, Y. Samson, A. Marty, B. Gilles, and A. Chamberod, J. Magn. Magn. Mater. **172**, 26 (1997).
[15] L. J. Cabri *et al.*, Can. Mineral. **12**, 21 (1973).
[16] M. Maret, M. Albrecht, J. Kohler, R. Poinsot, C. Ulhaq-Bouillet, J. Tonnerre, J. Berar, and E. Bucher, J. Magn. Magn. Mater. **218**, 151 (2000).
[17] B. Kaplan and G. Gehring, J. Magn. Magn. Mater. **128**, 111 (1993).
[18] J. P. Attane, Y. Samson, A. Marty, J. C. Toussaint, G. Dubois, A. Mougin, and J. P. Jamet, Phys. Rev. Lett. **93**, 257203 (2004).
[19] D. Halley, Y. Samson, A. Marty, P. Bayle-Guillemaud, C. Beigne, B. Gilles, and J. E. Mazille, Phys. Rev. B **65**, 205408 (2002).
[20] A. Thiele, J. Appl. Phys. **41**, 1139 (1970).